Available online at www.sciencedirect.com

ScienceDirect

Geochimica et Cosmochimica Acta 223 (2018) 21–35

Geochimica et Cosmochimica Acta

www.elsevier.com/locate/gca

Spatially-resolved isotopic study of carbon trapped in ~3.43 Ga Strelley Pool Formation stromatolites

David T. Flannery [a,*], Abigail C. Allwood [a], Roger E. Summons [b], Kenneth H. Williford [a], William Abbey [a], Emily D. Matys [b], Nicola Ferralis [c]

[a] Jet Propulsion Laboratory, California Institute of Technology, Pasadena, CA 91109, USA
[b] Department of Earth, Atmospheric and Planetary Sciences, Massachusetts Institute of Technology, MA 02139, USA
[c] Department of Materials Science and Engineering, Massachusetts Institute of Technology, Cambridge, MA 02139, USA

Received 7 February 2017; accepted in revised form 18 November 2017; Available online 24 November 2017

Abstract

The large isotopic fractionation of carbon associated with enzymatic carbon assimilation allows evidence for life's antiquity, and potentially the early operation of several extant metabolic pathways, to be derived from the stable carbon isotope record of sedimentary rocks. Earth's organic carbon isotope record extends to the Late Eoarchean-Early Paleoarchean: the age of the oldest known sedimentary rocks. However, complementary inorganic carbon reservoirs are poorly represented in the oldest units, and commonly reported bulk organic carbon isotope measurements do not capture the micro-scale isotopic heterogeneities that are increasingly reported from younger rocks. Here, we investigated the isotopic composition of the oldest paired occurrences of sedimentary carbonate and organic matter, which are preserved as dolomite and kerogen within textural biosignatures of the ~3.43 Ga Strelley Pool Formation. We targeted least-altered carbonate phases *in situ* using microsampling techniques guided by non-destructive elemental mapping. Organic carbon isotope values were measured by spatially-resolved bulk analyses, and *in situ* using secondary ion mass spectrometry to target microscale domains of organic material trapped within inorganic carbon matrixes. Total observed fractionation of ^{13}C ranges from −29 to −45‰. Our data are consistent with studies of younger Archean rocks that host biogenic stromatolites and organic–inorganic carbon pairs showing greater fractionation than expected for Rubisco fixation alone. We conclude that organic matter was fixed and/or remobilized by at least one metabolism in addition to the CBB cycle, possibly by the Wood-Ljungdahl pathway or methanogenesis-methanotrophy, in a shallow-water marine environment during the Paleoarchean.
© 2017 Elsevier Ltd. All rights reserved.

Keywords: Stromatolite; Archean; Planetary Instrument for X-ray Lithochemistry; PIXL; Strelley Pool Formation; SIMS; Carbon isotope

1. INTRODUCTION

The stable carbon isotope values of organic matter and inorganic carbon provide a record of biological carbon assimilation extending to the early Archean (Fig. 1). The direction and magnitude of isotopic offset between the two carbon reservoirs reflects the integrated fractionations imparted by all biological processes contributing to organic matter burial, as well as any diagenetic processes, hydrothermal alteration and regional metamorphism altering the isotopic composition of carbon-bearing phases. In Precambrian rocks, average total fractionations are remarkably consistent (ε = ~−26‰; Schidlowski, 1987) and are generally thought to reflect the early evolution and continuous operation of the Calvin-Benson-Bassham (CBB) cycle for carbon assimilation. In more recent studies, $\delta^{13}C_{org}$ values as low as −37‰ are interpreted in the context of the CBB cycle (e.g. Eigenbrode and Freeman, 2006).

* Corresponding author.
E-mail address: flannery@jpl.nasa.gov (D.T. Flannery).

https://doi.org/10.1016/j.gca.2017.11.028
0016-7037/© 2017 Elsevier Ltd. All rights reserved.

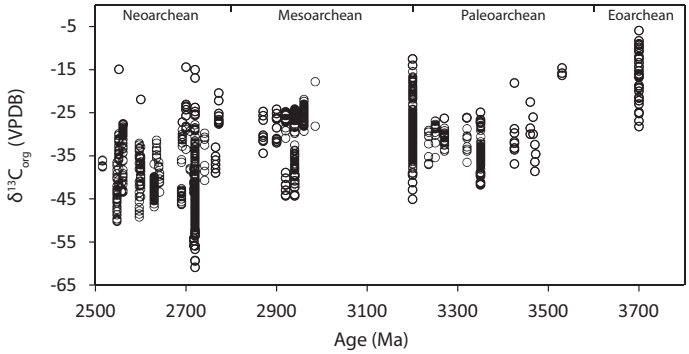

Fig. 1. Stable organic isotope values reported from Archean units, compiled from supplementary references and new data reported here.

However, greater fractionations are reported from some Precambrian units, most notably those deposited during the Neoarchean (Schidlowski, 1988). Highly ^{13}C-depleted Neoarchean values are widely interpreted as evidence for the activity of methane cycling microbial communities (Hayes, 1994). Archean methanogens and methanotrophs would have regulated atmospheric methane, possibly at comparatively high levels, which could have led to greenhouse warming that mitigated the reduced luminosity of the early sun (Pavlov et al., 2001). Methanogens may also have contributed to the rise of oxygen by producing CH_4 that underwent photolysis thereby allowing H_2 to escape to space preferentially (Catling et al., 2001). ^{13}C-depleted methane inclusions putatively preserved within hydrothermal precipitates of the Dresser Formation have been claimed as evidence for the evolution of methanogenesis prior to ~3.5 Ga (Ueno et al., 2006), but an abiological origin for these inclusions has also been proposed (Lollar and McCollom, 2006). Other circumstantial evidence for an early origin of methanotrophy includes the close phylogenetic relationship of archaeal methanotrophs and early-evolving methanogens (Hinrichs et al., 1999), and $\delta^{13}C_{org}$ values as low as -43‰ reported from Mesoarchean shale by Kiyokawa et al. (2006). Alternatively, these fractionations, which are greater than expected for fixation by D-ribulose-1,5-bisphosphate carboxylase/oxygenase (Rubisco) alone, could reflect CO_2 fixation via the Wood-Ljungdahl pathway (reductive acetyl-CoA pathway), which is generally considered capable of ^{13}C fractionations of −30 to −40‰ (Knoll and Canfield, 1998; Fischer et al., 2009). This pathway is employed by modern acetogenic bacteria in a process that culminates in ^{13}C fractionations of up to -69‰ in closed, laboratory-based systems (Freude and Blaser, 2016). Thus, it is conceivable the Wood-Ljungdhal pathway produced significant ^{13}C fractionations reported from Archean rocks. Regardless of the pathway(s) responsible, the timing of the evolution of metabolisms capable of greater fractionations than Rubisco remains poorly-known, primarily because paired occurrences of sedimentary carbonate and organic matter become increasingly rare in the early geological record. Here, we contribute new isotope data obtained from carbon sequestered in dolomite and organic matter associated with textural biosignatures in the ~3.43 Ga Strelley Pool Formation, the oldest known supracrustal carbonate sequence. Our dataset represents the oldest known paired occurrences of significant sedimentary carbonate and organic matter, and the oldest organic matter described from stromatolites. In order to select areas minimally-affected by isotopic shifts related to diagenesis, regional metamorphism and hydrothermal alteration, we targeted least-altered carbonate phases using microsampling techniques guided by non-destructive elemental mapping. Organic carbon isotope values were measured by bulk analyses and *in situ* by secondary ion mass spectrometry (SIMS).

2. GEOLOGICAL SETTING

The Strelley Pool Formation is an important stratigraphic marker within the early Archean Pilbara Supergroup, Western Australia. The Pilbara Supergroup was deposited during the Paleoarchean, contemporaneously with the development of a series of large granitoid bodies which now divide the Stelley Pool Formation (SPF) between 11 greenstone belts (Fig. 2). The SPF unconformably overlies volcanic and sedimentary rocks of the 3520–3427 Warrawoona Group and is unconformably overlain by ultramafic volcanic rocks of the 3350–3315 Ga Kelly Group (Hickman, 2008). It is locally up to 1 km thick and consists predominantly of sandstone, conglomerate, quartzite, volcaniclastic rocks and variably silicified sedimentary carbonate. The stratigraphy, sedimentology and trace element geochemistry suggest deposition occurred primarily within a shallow-water marine environment that was periodically influenced by hydrothermal fluids (Van Kranendonk et al., 2003; Hickman, 2008; Allwood et al., 2010). Biological activity during deposition of the unit is recorded by stromatolites (Allwood et al., 2006), biogenic isotopic fractionations (Wacey et al., 2010, 2011; Lepot et al., 2013) and microfossils (Sugitani et al., 2010, 2013; Wacey et al., 2011). Regional metamorphism in our study area was limited to greenschist facies (Hickman, 2008; Wacey, 2010).

3. METHODS

3.1. Fieldwork

Hand samples were collected from Strelley Pool Formation outcrop at Anchor Ridge in the North Pole Dome

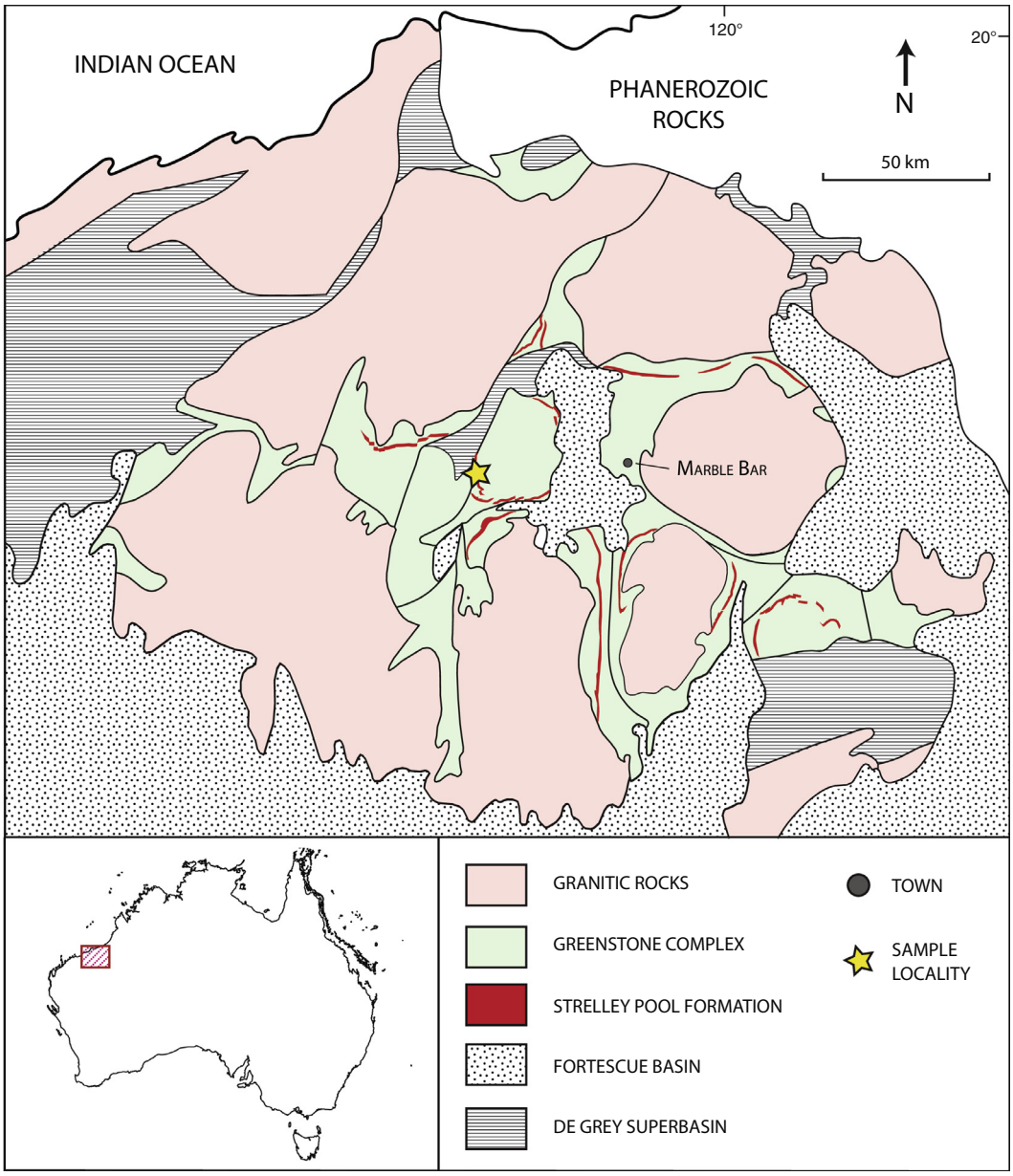

Fig. 2. Simplified geological map of the Pilbara Craton, Western Australia, showing Strelley Pool Formation outcrop and the locality sampled for this study. Geological boundaries after Hickman, 2008. Australia outline inset provided by Geoscience Australia.

(Fig. 2). Stratigraphic sections were measured using a Jacobs Staff, Abney level and measuring tape. Samples collected for geochemical analysis were obtained from grey-coloured, freshly-broken carbonate. Small samples were placed in fabric sample bags prior to transport and a large (~20 kg) conical stromatolite was shipped for subsequent sectioning.

3.2. Petrography

Light and electron microscopy, and energy dispersive X-ray spectroscopy were performed in the JPL Astrobiogeochemistry Laboratory (abcLab). Petrographic thin sections and SIMS targets were imaged in reflected, transmitted, cross-polarized and reflected UV light using a Leica DM6000 fitted with automated stages and software allowing for large area, high-resolution mosaicking. Scanning electron microscopy and energy dispersive spectroscopy (SEM-EDS) was performed using an Hitachi SU-3500 variable pressure SEM in secondary electron (SE) and backscattered electron (BSE) modes. We used SEM-EDS to investigate dolomite mineral phases and organic domains preserved within dolomitic laminae. Organic domains imaged using light microscopy were relocated and mapped using backscattered electrons and energy dispersive X-ray spectroscopy in order to confirm their composition and indigeneity. Images were typically acquired with an accelerating voltage of 5–30 kV and a

working distance of ~5 mm for best spatial resolution, or 10 mm for elemental analysis. Elemental mapping of SIMS targets at sub-μm resolution was achieved using an Oxford Instruments X-Max 150 mm^2 silicon drift energy dispersive spectroscopy system. SIMS targets, other organic domains and minerals were mapped using a benchtop confocal Horiba multi-wavelength Raman imaging spectrometer set up for long duration (30,000 spectra) mapping. A variant of the Planetary Instrument for X-ray Lithochemistry (PIXL; Allwood et al., 2015) was used to map the elemental composition of cut and polished slab surfaces with X-ray fluorescence, and to guide microsampling of dolomite phases, some of which are characterized by variable Fe content. X-rays were generated by a rhodium anode X-ray tube operating at 28 kV and focused to a 100 μm analytical spot by a glass polycapillary optic manufactured by XOS. The instrument was rastered across the scan area using an XYZ stage while fluoresced and scattered x-rays were detected by one or more Amptek silicon drift detectors. Data cubes were processed using Wavemetrics Igor software, which was also used to generate element intensity maps and summed spectra for selected rock components.

3.3. Microsampling

Hand samples were cut and polished using de-ionized water, diamond rock saws and alumina grit prior to being microsampled using a New Wave Research 101316 series micromill. Carbonate phases were identified *in situ* using SEM-EDS, micro-XRF and standard petrographic techniques applied to thin sections prepared from the faces of opposing slabs. Fresh scalpels and Teflon sample containers were used to remove and weigh micromill powders. Drill bits were cleaned with ethanol and slabs were sonicated between sampling runs. Samples were weighed using a Mettler Toledo XPE205 analytical balance prior to geochemical analyses.

3.4. Stable carbonate carbon and oxygen isotope analyses

Stable carbonate carbon and oxygen isotope analyses were performed at the University of Michigan Stable Isotope Laboratory. Micromilled carbonate samples weighing a minimum of 10 micrograms were placed in stainless steel boats prior to being heated to 200 °C in vacuum for one hour to remove volatile contaminants and water. Samples were then placed in individual borosilicate reaction vessels and reacted at 77° ± 1 °C with 4 drops of anhydrous phosphoric acid for 8 min in a Finnigan MAT Kiel IV preparation device coupled directly to the inlet of a Finnigan MAT 253 triple collector isotope ratio mass spectrometer. ^{17}O-corrected data were further corrected for acid fractionation and source mixing by calibration to a best-fit regression line defined by two NBS standards: NBS 18 and NBS 19. Precision and accuracy of data were monitored through daily analysis of a variety of powdered carbonate standards. All measured isotope ratio values are reported in standard delta (δ) notation where $\delta^{13}C = (R_{Sa}/R_{Std} - 1)‰$, and R_{Sa} and R_{Std} are the isotope ratio of the sample and the Vienna Pee Dee Belemnite (VPDB) isotope standard, respectively. Measured precision is better than 0.1‰ for both carbon and oxygen isotope compositions.

3.5. Bulk stable organic carbon isotope analyses

3.5.1. Materials

Solvents, reagents, and laboratory wares were cleaned thoroughly before use according to Hallmann et al. (2011) to remove all organic contaminants. Glassware and aluminum foil were combusted at 500 °C for 8 h. Quartz sand was combusted at 850 °C for 12 h. Solvents (*n*-hexane, methanol and dichloromethane) used in cleaning were of high purity grade (OmniSolv, EMD Chemicals). Milli-Q water and hydrochloric acid (HCl) used to process samples were cleaned by five liquid-liquid extractions with dichloromethane (DCM). Metal tools were cleaned with hexane, DCM, and methanol (MeOH). Crushing instruments were cleaned by grinding with baked quartz sand and by subsequent ultrasonication in DCM and MeOH. Polytetrafluorethylene (Teflon) products used in acid digestion were cleaned by boiling in hydrogen peroxide for 12 h.

3.5.2. Sample preparation

A conical stromatolite (sample identifier: 9-6-10-1) was sectioned into 6 layers cut perpendicular to the vertical axis of the structure. Each layer was cut into 4 quadrants. Quadrants were stored in combusted aluminum foil and handled sparingly to limit the potential for contamination. Two quadrants from each of the 6 layers (~25 mg each) and a bulk sample (~1 kg) were powdered for kerogen isolation using a ShatterBox puck mill. The puck mill was cleaned thoroughly between the powdering of samples as described above.

3.5.3. Kerogen isolation

Rock powders were demineralized by acidification in Teflon tubes that had been previously cleaned using hydrogen peroxide followed by solvents. The powders were then covered with 12 N HCl:Milli-Q water (1:1 (v:v); 6 N HCl) and the tubes were left for ~24 h, agitated periodically, after which the supernatants were decanted and fresh 6 N HCl was added to each Teflon tube. After the removal of all carbonates, the powders were neutralized using Milli-Q water. Silicates were removed through an aqueous hydrofluoric acid (HF) digestion. Rock powders were covered with HF. The tubes were agitated periodically and left for ~24 h, after which the supernatants were decanted and fresh HF was added. After the removal of all silicates the residues were neutralized using Milli-Q water. To ensure the removal of any fluoride-precipitates that may have formed, the isolated kerogens were treated again with 6N HCl for ~24 h. The isolated kerogens were suspended in Milli-Q water and pelleted by centrifugation. The supernatants were decanted and the kerogens were transferred to 4 ml vials filled with 9:1 DCM:MeOH. The kerogens were then dried and weighed.

3.5.4. EA-IRMS analyses

Rock powders for kerogen isotope measurements were demineralized as described above. Measurements were run

in triplicate with each measurement consuming 0.3–0.5 mg of isolated kerogen. Carbon isotopic compositions were determined using a Fisons Instruments NA 1500 NC elemental analyzer coupled to a Thermo-Finnigan Delta Plus XP isotope ratio mass spectrometer. Isotopic reference standards were obtained from Arndt Schimmelmann of Indiana University. Multiple MIT laboratory standards of acetanilide, sucrose, urea, a crude oil, atropine, cyclohexanone and a Neoarchean kerogen composite (Eigenbrode and Freeman, 2006) were also measured for calibration, normalization and TOC quantification. All analyses are reported in standard delta (δ) notation (‰, VPDB).

3.6. SIMS stable organic carbon isotope analyses

SIMS mounts were prepared from hand samples collected from Strelley Pool Formation outcrop. Analytical standards were top mounted in thin sections using a 0.3 mm drill bit mounted to a computer controlled micromill. Standards were placed in micromilled holes using tweezers and epoxied in place prior to an additional round of polishing using alumina. After petrographic work and target acquisition using light microscopes and variable pressure SEM modes, and immediately prior to SIMS analysis, mounts were coated with ~100 nm of gold and allowed to degas for 12 h in the 108 torr vacuum of the WiscSIMS instrument airlock. We generally followed the SIMS techniques described by Kita et al. (2009), Valley and Kita (2009), Williford et al. (2016, 2011) and Ushikubo et al. (2014). The small nature of organic domains and the presence of C in the surrounding carbonate matrix necessitated a <6 μm beam and sub-μm beam positioning accuracy. Analyses of organic C in an inorganic C matrix is possible due to the low C-production in carbonate relative to organic carbon. Carbonate carbon did not contribute significantly to SIMS measurements of organic domains because it has a significantly lower ionization efficiency compared to organic carbon, and dolomite is 13% C by mass compared to 60–>90% C by mass for sedimentary organic matter. During analyses, a primary beam of 133Cs+ was focused on the surfaces of samples. Beam diameter varied by <1 μm, and intensity varied depending upon instrument conditions. Total impact energy was maintained at 20 keV and the secondary-ion accelerating voltage was maintained at 10 keV. An electron gun oriented normal to the sample surface, and the gold coating applied to the sample, provided charge compensation. Secondary ions of the major and minor C isotopes were collected using Faraday cup detectors. Hydride ions (e.g. ^{13}CH) were measured simultaneously. Each analysis consisted an interval for (i) pre-sputtering to penetrate the gold coating and any minor surface contamination, (ii) centering secondary ions in the field aperture, and (iii) isotope ratio measurement. Correction for the sum of mass fractionation effects internal to the SIMS instrument (bias) was achieved using the following alpha correction:

$$\alpha = (1000 + \delta^{13}C_{raw})/(1000 + \delta^{13}C_{True})$$

Here, α is bias, $\delta^{13}C_{raw}$ is the uncorrected value for a standard analysis, and $\delta^{13}C_{True}$ is the value for the standard as determined by conventional, gas-source isotope ratio mass spectrometry. Each set of ~10 unknown sample analyses was bracketed by four analyses of a working standard (UWLA-1) top mounted into the specimen. Bias and external precision are defined for each bracket as the average α, and two standard deviations (2SD, expressed in permil) of the eight standard analyses, respectively. Internal precision is defined as two standard errors (2SE) of the individual isotope ratios calculated from multiple measurement cycles within each analysis. Average count rates for the major ion (^{12}C) were also calculated using the multiple measurement cycles performed during each analysis, and are reported as a percentage relative to the average for the eight bracketing standard analyses as $^{12}C_{rel}$. Using a protocol described by Williford et al. (2016) for data quality assurance when measuring mixed phases at low count rates (see Fig. S4), we rejected analyses with total ^{12}C counts less than 20% of the average value obtained from the top-mounted standard (5.7×10^7 counts).

Bias correction was supplemented by an additional correction for H/C using standards and values measured using gas-source isotope ratio mass spectrometry (Williford et al., 2016). At the beginning of each SIMS session, six of the standards (Baltic Amber, SH95S1a, UWHA-1, UWJA-1, UWLA-1, UWMA-1) were analyzed multiple times, bracketed by analyses of the primary working standard UWLA-1. Mass 14 (^{13}CH) was measured simultaneously with ^{12}CH and ^{13}CH and used to calculate $^{13}CH/^{13}C$. A linear regression was calculated using differential bias (α^*, or the ratio of the bias for a given organic standard to the bias for four bracketing analyses of UWLA-1) and $^{13}CH/^{13}C$. Differential bias is defined as the ratio of bias for each calibration standard to bias for UWLA-1 during the calibration routine. This method permits calculation of α^* for each sample analysis using $^{13}CH/^{13}C$. For each $\delta^{13}C$ analysis of organic matter in dolomitic laminae, total bias correction was achieved using the following equation:

$$\delta^{13}C = (1000 + \delta^{13}C_{raw})/(\alpha \times \alpha^*) - 1000$$

In order to confirm the location of SIMS analyses, we removed the gold coat applied to mounts using cyanide in a process based on that described by Leslie and Mitchell (2007), and then acquired SEM images of SIMS pits. SIMS mounts were lightly polished using 0.1 μm alumina on a nylon pad to remove the majority of the gold coat. Mounts were then placed in a ~10 cm diameter glass jar on a cardboard platform above ~1 g of potassium cyanide wrapped in a wet paper towel. The jar lid was sealed using parafilm and the jar was left to sit for 3 days in a fume hood, during which time water vapor and hydrogen cyanide gas were produced, and the gold was mobilized in $Au(CN)_2^-$ ions. SIMS mounts were removed from the jar and rinsed with de-ionized water prior to sonication for 2 min in a beaker filled with ethanol, and then again for 2 min in de-ionized water. The mounts were dried using ultrapure nitrogen gas prior to SEM imaging using backscattered electron modes to confirm the gold coat had been removed. A 3 nm platinum-palladium coat was reapplied for final SEM pit imaging.

3.7. Micro-Raman Spectroscopy

Experimental micro-Raman spectra were acquired using an Horiba LabRAM 800 HR spectrometer equipped with a He-Ne (632.817 nm) laser as the excitation source and a Peltier-cooled CCD detector. The laser was focused on the sample with a 400 nm confocal hole using the 100X objective under reflected illumination. The laser spot on the sample was ~800 nm in diameter and had a power of ~0.4 mW or below at the sample surface. A calibrated edge high band filter (lowest wavenumber: ~70 cm^{-1}) was used to minimize the elastic backscattered signal. A minimum of 10 independent spots were analyzed on each sample and data were collected from 5 to 60 s per spot depending upon the Raman/fluorescence intensity. The full spectral window for each acquisition was −50 to 4000 cm^{-1}. To reduce the amount of artifacts introduced by subtraction of the highly non-linear background over the full spectra, the spectra were broken down into several regions of interest. The first-order spectral window for the organic region was taken from 1000 to 1800 cm^{-1}. The background subtraction in this spectral window was performed using 2th order polynomial functions within the selected region. Peak fitting was carried out using Horiba LabSpec5. Spectral fitting was carried out based on Ferralis et al. (2016). The fit was initialized with the inclusion of the D4, D5, D1, D3, G + D2 peaks (with initialization positions at: 1150, 1260, 1330, 1450, 1580 and 1600 cm^{-1}, respectively). The maximum allowed peak width was 100 cm^{-1}. If D2 was discernible from G a separate peak was fit at 1600 cm^{-1}, otherwise the peak was denoted as "G" representing the cumulative G + D2. The optimal peak fit was achieved when the standard error between the fit result and the raw data converged to its smallest value (the converged standard error varied depending on the level of noise in each spectra). The peaks at 1400 and 1500 were reduced to a single peak during the fitting if that led to a lower standard error. Peak fitting was carried out using PseudoVoigt profiles, a linear combination of a Gaussian and a Lorentzian. Peak intensities were averaged over multiple acquisitions for the extraction of peak intensity ratios.

4. RESULTS

4.1. Petrography

Field observations indicate the microsampled slabs (Fig. 3) belong to diverse facies. Samples 10-7-07–6a, 9-6-10-1-slab1, IBO-4, 9-7-07-2b and 13-7-07-2a represent stromatolitic material. Sample 10-7-07-4a is a slab prepared from a unit of acicular crystal pseudomorphs. Thin section optical light petrography, as well as SEM-EDS and micro-XRF analyses, suggest all samples consist of dolomite and chert interlaminated on a μm to mm scale (Fig. 4). The laminated chert is petrographically diverse. Microfabrics and inclusions suggest it likely originated in multiple phases of post-depositional silicification of sedimentary carbonate. Cross-cutting black chert veinlets visible in some polished slabs and thin sections are related to syndepositional hydrothermal activity (Van Kranendonk, 2006; Sugitani et al., 2015). Three dolomite phases comparable to those previously described by Allwood et al. (2009) were identified in thin sections and in cut slabs. D1 consists of recrystallized, equigranular, anhedral dolomite crystals in a sutured mosaic. D2 consists of very fine-grained anhedral crystals occurring around the margins of larger dolomite crystals, at the centers of D1 laminae, and at the contacts between chert and dolomitic laminae. D3 consists of equigranular, euhedral dolomite rhombs exhibiting overgrowths that are visible in transmitted light and backscattered electron SEM modes. Laminae composed predominantly of D3 dolomite are typically discernable in cut slabs as lighter-toned zones, and as zones of higher iron content in micro-XRF and SEM-EDS element maps (Supplementary Figures S1–S3).

Domains of organic matter (OM) targeted by our SIMS analyses range in size from 1 to 10 μm and occur at the boundaries of D2 dolomite crystals in sample 9-7-07-2b. These zones are restricted to the triple points of D2 dolomite crystals in two ~1 mm thick laminae, where the OM is often associated with μm-scale aggregates of a Ti-rich mineral, possibly rutile. OM also occurs in oxidized fractures associated with areas of recent weathering. When examined in highly-polished thin sections, organic domains occurring within D2 dolomite laminae appear black in transmitted light and yellow in reflected light. All SIMS targets were confirmed using transmitted and reflected light microscopy and SEM-EDS. Epoxy-filled holes also occur in our SIMS mounts, but can be distinguished from indigenous OM by their clear appearance in transmitted light and the presence of a Cl peak in SEM-EDS spectra. Inclusions of dolomite, silica, sulfides and iron oxides are present in some organic domains, but we did not recognize textural categories of OM based on observations made using reflected light or scanning electron microscopy.

4.2. Microsampled stable carbonate carbon and oxygen isotope data

The results of stable carbonate carbon and oxygen isotope analyses are shown in Fig. 5 and Table 1. Carbonate $\delta^{13}C$ data range +1.8 to +3.1‰ and cluster around a mean of +2.8‰, which is significantly heavier than values obtained for the majority of Precambrian carbonates deposited in open marine conditions (Shields and Veizer, 2002). Significant deviations towards lighter values occur in laminae containing D3 dolomite.

Our $\delta^{18}O$ values range from −15.4 to −9.4‰, which is similar to values obtained from many other Precambrian carbonate platforms (Shields and Veizer, 2002). There is a strong correlation between low $\delta^{13}C$ and low $\delta^{18}O$ values obtained from D3 dolomite layers, suggesting some resetting of $\delta^{18}O$ values by diagenetic fluids and/or remineralization of highly ^{13}C-depleted organic matter (cf. Fischer et al., 2009).

4.3. Bulk stable organic carbon isotope data

The results of spatially-resolved, bulk stable organic carbon isotope analyses are shown in Fig. 6 and Table 2. Organic $\delta^{13}C$ data range −33.6 to −26.1‰ and average −28.5‰. The standard deviation from the mean for

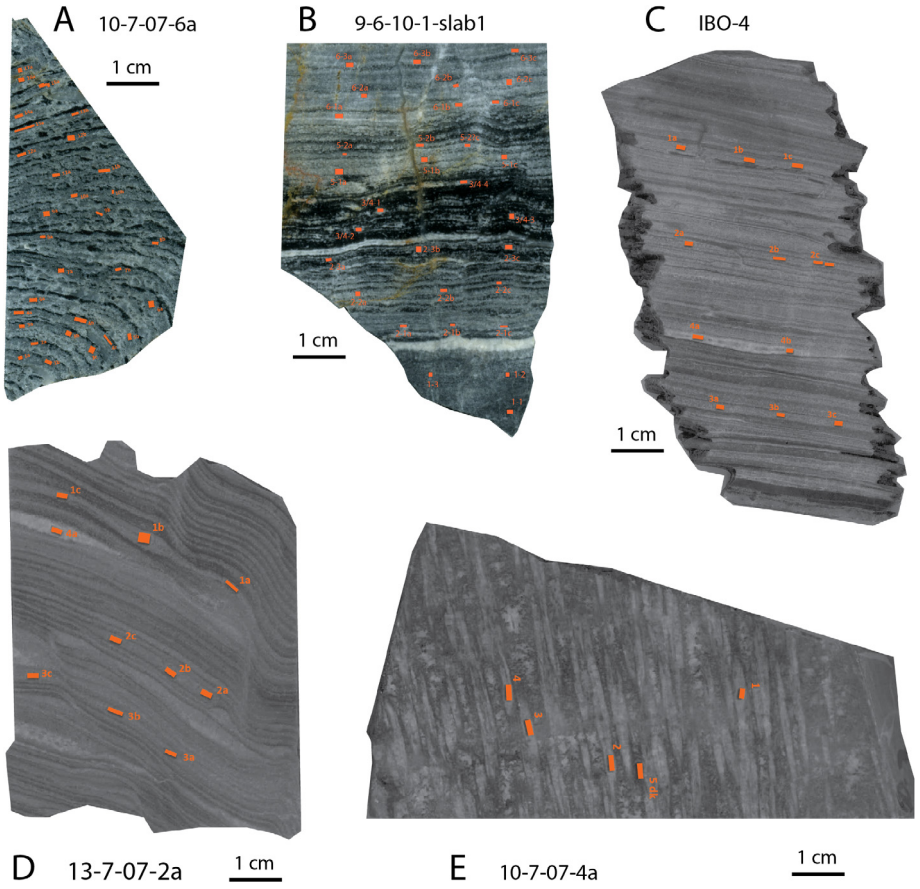

Fig. 3. Outcrop sketch showing the location of hand sampling (A) and microsampling locations shown in cut and polished slabs collected from outcrop (B-F).

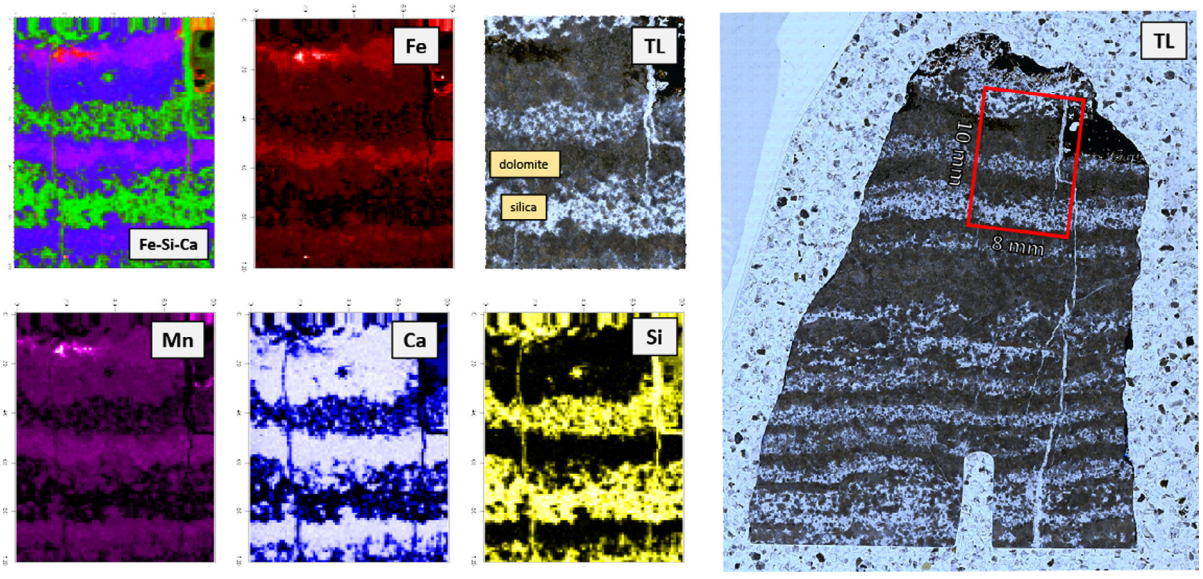

Fig. 4. Petrographic thin section shown in transmitted light (TL) and in element intensity maps obtained using micro-XRF. Note the alternating Si- (silica) and Ca-rich (dolomitic) laminae. D3 (secondary) dolomite is visible as areas enriched in Fe.

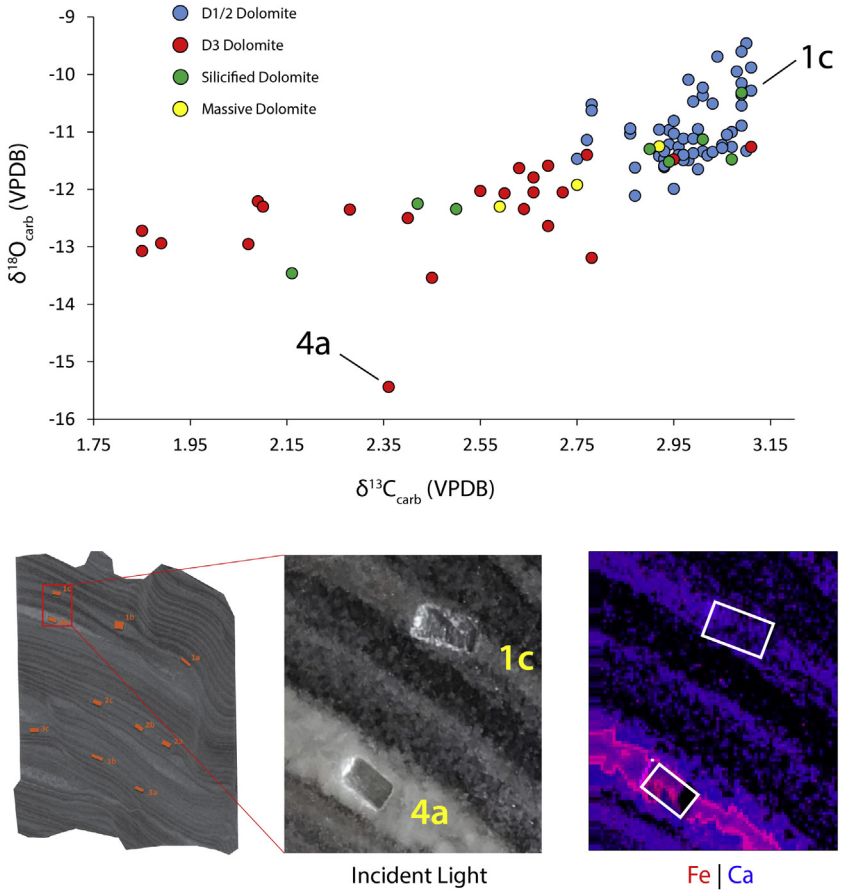

Fig. 5. Above: $\delta^{13}C/\delta^{18}O$ scatter plot showing the distribution of stable isotope values for microsampled dolomite phases. Below: Micro-XRF element intensity map showing Fe-enriched secondary (D3) dolomite in the area of microsample pit 4a. This sample yielded significantly depleted ^{13}C and ^{18}O carbonate isotope values. The width of the micro-XRF map is 8 mm.

kerogen samples reaches 1.34‰ due primarily to outliers that are present in each sample set. However, the standard deviation from the mean for all analytical standards (Arndt acetanilide, sucrose, urea, crude oil, atropine, and cyclohexanone) is less than 0.19‰.

4.4. SIMS stable organic carbon isotope analyses

We measured organic domains present at the triple junctions of D2 dolomite in two dolomitic laminae separated by silica-rich laminae in a SIMS mount prepared from hand sample 9-7-07-2B (Fig. 7). A total of 100 analyses were made on 77 targets (Supplementary Figs. 7 & 8; Supplementary Table 2). Analyses where ^{12}C count rates exceeded 20% of the average count rate obtained for analyses of the anthracite standard are shown in Fig. 8. Of the 75 analyses exceeding this threshold, 67 achieved sub-permil internal precision. The remaining 9 analyses, which are closer to the 20% count rate threshold, achieved an internal precision of 1–1.6‰ ±2SE. Poorer internal precision is also associated with heterogeneity at depth within the target. 64 of the analyses exceeding the count rate threshold achieved sub-permil external precision, and the remaining 11 achieved an external precision of 1–1.7‰. $\delta^{13}C_{org}$ values obtained by SIMS range −32 to −42‰. Most of our values cluster around a mean of −35‰. However, a bimodal distribution is suggested by an additional population of lower values (Supplementary Fig. 7). Isotopic differences were not observed to correlate with inclusions or textural differences (Supplementary Fig. 8). The high external precision of analyses (±1‰, 2 SD) compared to the 10‰ range of $\delta^{13}C_{org}$ values suggests that most of the observed isotopic variation represents natural heterogeneity in Strelley Pool Formation organic matter rather than analytical artifacts. Where multiple analyses were made of the same organic domain, intra-domain variability is at most 1.9‰.

4.5. Micro-Raman spectroscopy and structural homogeneity

Microscale spatial resolution afforded by laser Raman spectroscopy allowed characterization of chemical and structural heterogeneity of kerogen across and within subcomponents of sample '9-6-10-1 SLAB-1' (Fig. 9). The degree of chemical and structural variability was quantified through the analysis of individual spectral features extracted from optimized peak fitting. D4 + D5/G values are reported in Table 2. Some of the subcomponents (for example subsamples /4/SE and 5/SE, Supplementary Fig-

Table 1
Stable inorganic carbon and oxygen isotope values obtained for micromilled samples.

Sample	Mineralogy	$\delta^{13}C$ (VPDB)	$\delta^{18}O$ (VPDB)
10-7-07-6A-SLAB2A DL-1a	D1/2 dolomite	3.07	−11.26
10-7-07-6A-SLAB2A DL-1b	D1/2 dolomite	2.95	−11.99
10-7-07-6A-SLAB2A DL-2a	D1/2 dolomite	2.98	−11.49
10-7-07-6A-SLAB2A DL-3a	D1/2 dolomite	2.93	−11.61
10-7-07-6A-SLAB2A DL-3b	D1/2 dolomite	2.94	−11.22
10-7-07-6A-SLAB2A DL-3c	D1/2 dolomite	2.92	−11.42
10-7-07-6A-SLAB2A DL-4a	D1/2 dolomite	2.93	−11.47
10-7-07-6A-SLAB2A DL-4b	D1/2 dolomite	2.94	−10.97
10-7-07-6A-SLAB2A DL-4c	D1/2 dolomite	2.75	−11.47
10-7-07-6A-SLAB2A DL-5a	D1/2 dolomite	2.86	−11.03
10-7-07-6A-SLAB2A DL-5b	D1/2 dolomite	2.96	−11.26
10-7-07-6A-SLAB2A DL-6a	D1/2 dolomite	2.97	−11.12
10-7-07-6A-SLAB2A DL-7a	D1/2 dolomite	3.05	−11.23
10-7-07-6A-SLAB2A DL-7b	D1/2 dolomite	3.01	−11.34
10-7-07-6A-SLAB2A DL-8a	D1/2 dolomite	2.93	−11.34
10-7-07-6A-SLAB2A DL-8b	D1/2 dolomite	3.09	−10.54
10-7-07-6A-SLAB2A DL-9a	D1/2 dolomite	2.93	−11.59
10-7-07-6A-SLAB2A DL-9b	D1/2 dolomite	2.97	−11.49
10-7-07-6A-SLAB2A DL-10a	D1/2 dolomite	3.02	−11.41
10-7-07-6A-SLAB2A DL-10b	D1/2 dolomite	3.07	−11.00
10-7-07-6A-SLAB2A DL-11a	D1/2 dolomite	3.09	−10.89
10-7-07-6A-SLAB2A DL-11b	D1/2 dolomite	3.00	−10.95
10-7-07-6A-SLAB2A DL-12a	D1/2 dolomite	2.96	−11.40
10-7-07-6A-SLAB2A DL-12b	D1/2 dolomite	3.03	−11.35
10-7-07-6A-SLAB2A DL-13a	D1/2 dolomite	3.10	−11.33
10-7-07-6A-SLAB2A DL-13b	D1/2 dolomite	2.99	−11.37
10-7-07-6A-SLAB2A DL-14a	D1/2 dolomite	2.87	−11.62
10-7-07-6A-SLAB2A DL-15a	D1/2 dolomite	2.77	−11.14
10-7-07-6A-SLAB2A DL-16a	D1/2 dolomite	3.05	−11.28
10-7-07-6A-SLAB2A DL-17a	D1/2 dolomite	2.97	−11.40
9-6-10-1 SLAB 1 1-1	Massive dol.	2.92	−11.25
9-6-10-1 SLAB 1 1-2	Massive dol.	2.75	−11.92
9-6-10-1 SLAB 1 1-3	Massive dol.	2.59	−12.30
9-6-10-1 SLAB 1 2-1a	D1/2 dolomite	3.00	−11.65
9-6-10-1 SLAB 1 2-1b	D1/2 dolomite	2.92	−10.96
9-6-10-1 SLAB 1 2-1c	D1/2 dolomite	2.87	−12.11
9-6-10-1 SLAB 1 2-2a	D3 dolomite	2.78	−13.19
9-6-10-1 SLAB 1 2-2b	D1/2 dolomite	2.99	−11.12
9-6-10-1 SLAB 1 2-2c	D1/2 dolomite	3.06	−11.05
9-6-10-1 SLAB 1 2-3a	Silicified dol.	2.94	−11.52
9-6-10-1 SLAB 1 2-3b	Silicified dol.	2.90	−11.30
9-6-10-1 SLAB 1 2-3c	Silicified dol.	3.01	−11.13
9-6-10-1 SLAB 1 3/4-1	Silicified dol.	2.50	−12.34
9-6-10-1 SLAB 1 3/4-2	Silicified dol.	2.42	−12.25
9-6-10-1 SLAB 1 3/4-3	Silicified dol.	3.09	−10.32
9-6-10-1 SLAB 1 3/4-4	Silicified dol.	3.07	−11.48
9-6-10-1 SLAB 1 5-1a	D3 dolomite	2.95	−11.48
9-6-10-1 SLAB 1 5-1b	D3 dolomite	2.09	−12.21
9-6-10-1 SLAB 1 5-1c	D3 dolomite	2.60	−12.07
9-6-10-1 SLAB 1 5-2a	D3 dolomite	3.11	−11.26
9-6-10-1 SLAB 1 5-2b	D3 dolomite	2.40	−12.50
9-6-10-1 SLAB 1 5-2c	D3 dolomite	2.77	−11.40
9-6-10-1 SLAB 1 6-1a	D3 dolomite	2.07	−12.95
9-6-10-1 SLAB 1 6-1b	D3 dolomite	1.85	−12.72
9-6-10-1 SLAB 1 6-1c	D3 dolomite	2.10	−12.30
9-6-10-1 SLAB 1 6-2a	D3 dolomite	2.66	−11.79
9-6-10-1 SLAB 1 6-2b	D3 dolomite	2.28	−12.35
9-6-10-1 SLAB 1 6-2c	D3 dolomite	1.85	−13.07
9-6-10-1 SLAB 1 6-3a	D3 dolomite	2.64	−12.34
9-6-10-1 SLAB 1 6-3b	D3 dolomite	2.69	−11.59
9-6-10-1 SLAB 1 6-3c	D3 dolomite	1.89	−12.94

(*continued on next page*)

Table 1 (*continued*)

Sample	Mineralogy	$\delta^{13}C$ (VPDB)	$\delta^{18}O$ (VPDB)
10-707-4a #1	D3 dolomite	2.66	−12.05
10-707-4a #2	D3 dolomite	2.63	−11.63
10-707-4a #3	D3 dolomite	2.55	−12.03
10-707-4a #4	D3 dolomite	2.72	−12.05
10-707-4a 5dk	Silicified dol.	2.16	−13.46
1B04-1a	D1/2 dolomite	2.78	−10.52
1B04-1b	D1/2 dolomite	3.03	−10.51
1B04-1c	D1/2 dolomite	2.99	−10.47
1B04-2a	D1/2 dolomite	3.01	−10.37
1B04-2b	D1/2 dolomite	3.09	−10.35
1B04-2c	D1/2 dolomite	2.78	−10.63
1B04-3a	D1/2 dolomite	2.86	−10.94
1B04-3b	D1/2 dolomite	2.95	−11.03
1B04-3c	D1/2 dolomite	2.95	−10.81
1B04-4a	D3 dolomite	2.45	−13.54
1B04-4b	D3 dolomite	2.69	−12.64
13-7-07-2a 1a	D1/2 dolomite	3.09	−10.15
13-7-07-2a 1b	D1/2 dolomite	3.11	−9.88
13-7-07-2a 1c	D1/2 dolomite	3.11	−10.28
13-7-07-2a 2a	D1/2 dolomite	3.10	−9.46
13-7-07-2a 2b	D1/2 dolomite	3.09	−9.60
13-7-07-2a 2c	D1/2 dolomite	3.04	−9.69
13-7-07-2a 4a	D3 dolomite	2.36	−15.44
13-7-07-2a 3a	D1/2 dolomite	3.08	−9.95
13-7-07-2a 3b	D1/2 dolomite	2.98	−10.09
13-7-07-2a 3c	D1/2 dolomite	3.01	−10.23

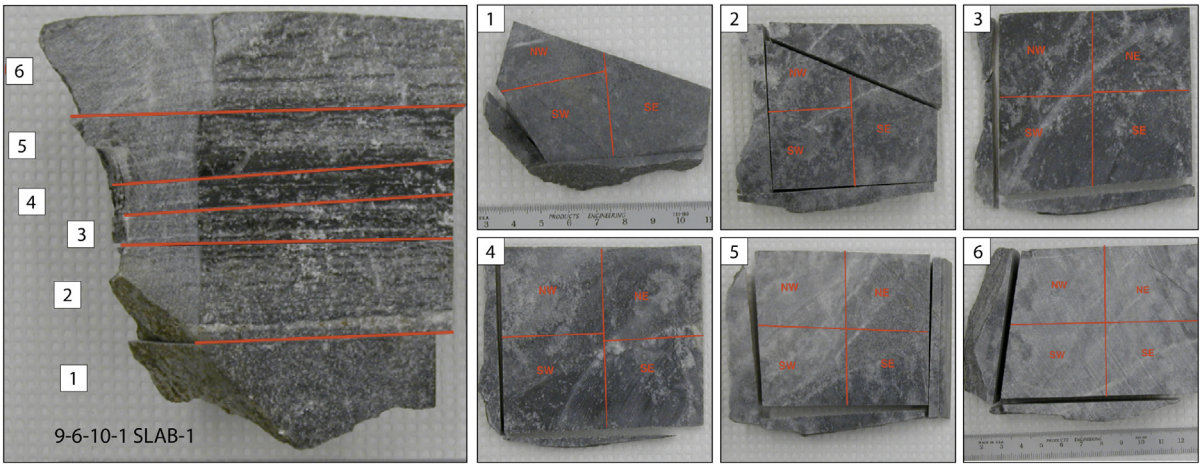

Fig. 6. Sub-sampling of sample "9-6-10-1 SLAB-1" for stable organic carbon isotope analyses.

ure 10) exhibit spectral variations consistent with chemical and structural variability. The latter is particularly noticeable when comparing G bands with distinctly different full-width half maxima (FWHM). Rather than a continuous range of FWHM values, two groups can be broadly identified based on the FWHM of the G peak (Group 1: ~63 1/cm; Group 2: ~45 1/cm). While some subcomponents exhibit only OM of group 1 (such as subsamples /1/SE and 2/SE), others have both (subsamples /1/NW, 2/NW, /4/SE, 5/SE and /6/SE) or only group 2 (subsamples /4/NW, /5/NW and /6/NW). FWHM values for the G band for group 1 are significantly higher than those in semigraphitic carbon (below ~45 1/cm, (Yoshida et al., 2006; Maslova et al., 2012; Rantitsch et al., 2016), precluding the possibility of stacking, while those in group 2 are close to the values expected for turbostratic graphite, suggesting the presence of initial stacking. Based on the observed difference in the width of the G band, the two groups have different aromatic cluster sizes, which can be quantitatively estimated for $(FWHM)_G$ below ~50 1/cm to be about ~10 nm, such as that in group 2 (Maslova et al., 2012). For both groups, the D1/G intensity ratios are significantly larger (in excess of 2) than that of high maturity anthracite or semigraphite, which have values <

Table 2
Stable organic carbon isotope values and D4+D5/G values from Raman spectra obtained from subcomponents of sample "9-6-10-1 SLAB-1".

Sample/Layer/Quad.	$\delta^{13}C$ (VPDB)	Stdev. $\delta^{13}C$	(D4+D5)/G
9-6-10-1-slab1/1/NW	−28.24	0.74	0.258
9-6-10-1-slab1/1/SE	−26.44	0.53	0.406
9-6-10-1-slab1/2/NW	−28.35	0.39	0.301
9-6-10-1-slab1/2/SE	−26.11	1.46	0.268
9-6-10-1-slab1/3/NW	−29.08	0.31	0.358
9-6-10-1-slab1/3/SE	−33.55	0.13	0.298
9-6-10-1-slab1/4/SE	−27.29	0.50	0.321
9-6-10-1-slab1/4/NW	−30.75	0.09	0.316
9-6-10-1-slab1/5/SE	−28.13	0.33	0.504
9-6-10-1-slab1/5/NW	−27.35	0.23	0.319
9-6-10-1-slab1/6/SE	−27.85	0.77	0.340
9-6-10-1-slab1/6/NW	−28.73	0.22	0.346
9-6-10-1-slab1/bulk	−28.14	0.07	0.317

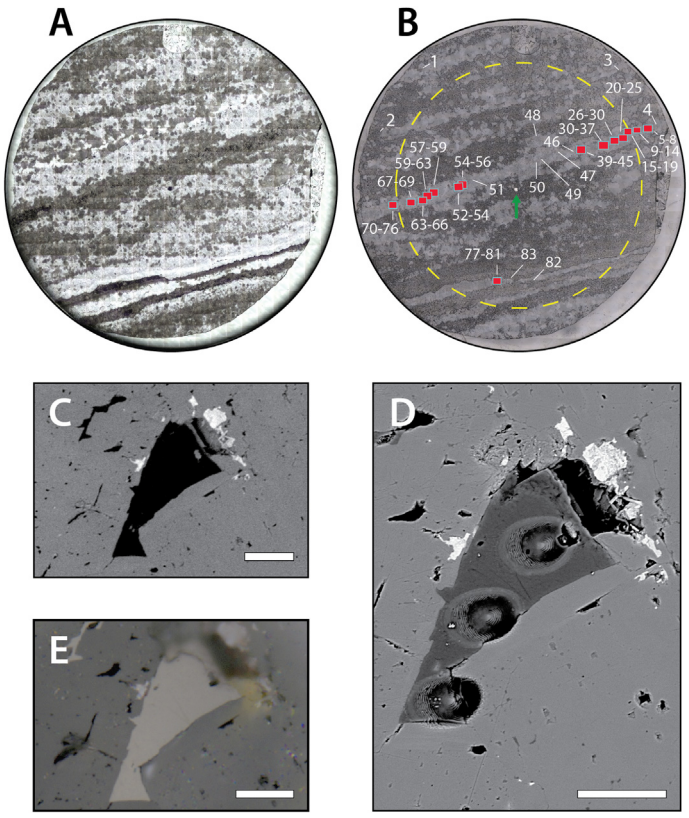

Fig. 7. The mount used for SIMS analyses shown in reflected (A) and transmitted (B) light. Numbers and lines show the location of organic domains corresponding to target numbers in SIMS analysis identifiers. The dashed yellow circle is the approximate area accessible to the SIMS instrument while maintaining acceptable precision and accuracy. The green arrow shows the location of top-mounted anthracite standard UWLA-1. A representative SIMS target (#25) is shown in reflected light (E) and backscattered electron mode under SEM prior to (C) and after (D) SIMS analysis. All scale bars = 10 μm. (For interpretation of the references to colour in this figure legend, the reader is referred to the web version of this article.)

1 (Rantitsch et al., 2016). Regardless of the size of aromatic clusters in each group, both exhibit a significant degree of disorder within the aromatic clusters, possibly in the form of carbon elemental substitution, or vacancies and defects with average distances between defects of the order of 1–2 nm (Lucchese et al., 2010).

5. DISCUSSION

5.1. Diagenetic alteration of carbonate carbon isotope values

Tucker (1982) suggested that much Archean dolomite may have precipitated directly from Archean seawater.

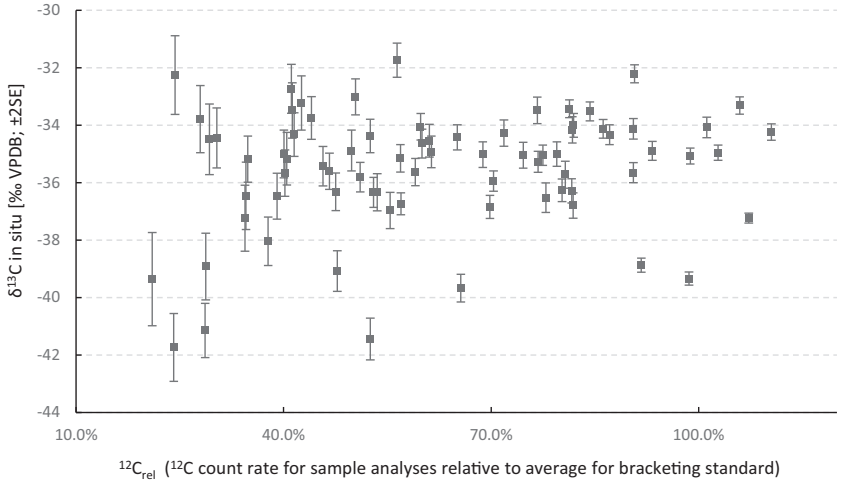

Fig. 8. SIMS $\delta^{13}C$ data for all analyses reported plotted against the ^{13}C count rate relative to an anthracite bracketing standard (UWLA-1). Error bars show internal precision (± 2 standard error).

Alternatively, it is often suggested that dolomitization occurs during early diagenesis in the presence of ground water with an isotopic composition comparable to seawater (Veizer and Hoefs, 1976). The interlocking nature of the dolomite crystals studied here, as well as growth rims and mineral inclusions, indicate that all of the dolomite in our samples has been recrystallized to some degree. However, the $\delta^{13}C$ values we obtained for D1/2 dolomite may still record the isotopic influence of Archean seawater. Our D1/2 dolomite $\delta^{13}C_{carb}$ values cluster around a mean (+3.0‰) that is heavier than typical values obtained from carbonate precipitated in open marine settings throughout the geological record [the global mean is close to ~0‰ (Shields and Veizer, 2002)]. Because diagenesis typically shifts $\delta^{13}C_{carb}$ toward more depleted values driven by isotopic re-equilibration with organic carbon, positive $\delta^{13}C_{carb}$ values are often interpreted as representing restricted marine environments wherein biological productivity sequestered significant ^{12}C sourced from the local DIC pool (cf. Melezhik et al., 2001). This interpretation is consistent with sedimentological evidence for partially restricted conditions during deposition of this part of the Strelley Pool Formation (i.e. The meter-scale units of pseudomorphed evaporite minerals first reported by Allwood et al., 2007).

5.2. Possible sources of organic matter

There is little debate as to the origin of organic matter present in younger stromatolites, where laminar accumulations of organic carbon are typically interpreted as having derived from a microbial mat that was present during accretion of the microbial sedimentary structure. However, the

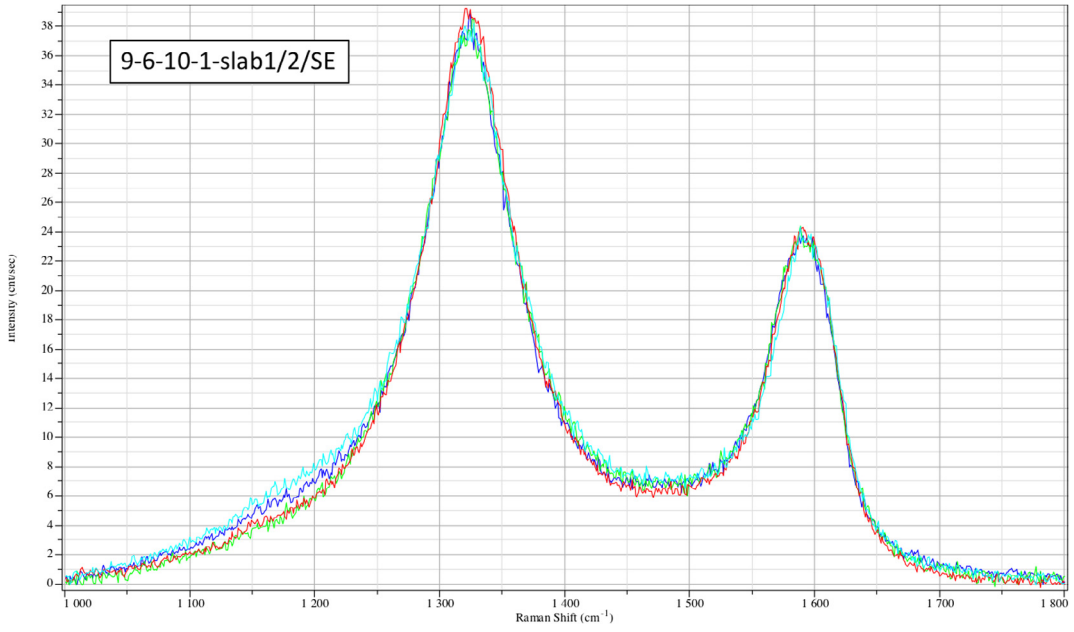

Fig. 9. Representative set of micro-Raman spectra from sample 9-6-10-1-slab1/2/SE acquired at different positions within the sample.

great age of SPF stromatolites, their very low organic carbon content, and evidence for hydrothermal activity that could have provided an alternative source of reduced carbon (Lindsay et al., 2005) introduces elements of ambiguity to this interpretation. The biogenicity of SPF stromatolites was questioned by Lowe (1980), who was the first to describe stromatolites of the Strelley Pool Formation and initially considered them biogenic, but later became a prominent sceptic (Lowe, 1994). Hofmann et al. (1999) argued for biogenicity based on morphological complexity (e.g. branching columns) and comparison to younger stromatolites (e.g. *Jacutophyton*). Subsequent detailed studies by Allwood et al. (2009, 2010, 2006) focusing on facies-controlled morphological variations, as well as textural and geochemical evidence, have led to a general consensus in favour of a biological origin. More recently, microfossils were described from SPF sandstone (Sugitani et al., 2010) and globular organic material was reported from silicified SPF stromatolites by Wacey (2010) and Duda et al. (2016). Lepot et al. (2013) used SIMS to measure the isotopic composition of carbon trapped within silica matrixes in samples collected from the SPF. They reported a −28 to −40‰ range of $\delta^{13}C_{org}$ values and suggested multiple metabolic inputs. In this work, we show that some OM also occurs in laminar accumulations within stromatolitic carbonate and that it is concentrated within dolomite phases that predate silicification and recent weathering. The spectral characteristics of OM obtained via Raman spectroscopy are consistent with greenstone facies metamorphism. We thus consider the organic matter we observed within SPF stromatolites to be indigenous, and, like OM reported from younger stromatolites, likely derived from a microbial mat that was present during accretion. Alternatively, a significant fraction of the organic matter may be derived from allochthonous sources, such as synsedimentary exhalative hydrothermal activity. Large, cross-cutting black chert veins that are rich in organics terminate elsewhere within the formation (e.g. Oehler et al., 2009), although they were not observed in the outcrop sampled for this study.

5.3. Isotopic evidence for multiple metabolic inputs

The generally consistent ($\varepsilon = \sim -26‰$; Schidlowski, 1987) isotopic composition of organic matter reported from sedimentary rocks throughout the geological record is widely accepted as evidence for the early evolution and continuous operation of autotrophy. New data reported here, which includes the oldest reported synsedimentary inorganic–organic carbon isotope pairs from a significant carbonate succession, includes bulk $\delta^{13}C_{org}$ values clustering around a mean of −28.5‰, which is typical for Rubisco-based metabolism. However, these values do not definitively show that microbes fixing carbon via the Calvin cycle contributed the majority of organic material to burial, as other metabolisms (e.g. the acetyl-CoA pathway) can produce similar fractionations. Furthermore, many of our data points suggest greater fractionation than expected for Rubisco fixation alone. OM input from multiple metabolic pathways is indicated by the microscale isotopic variability of OM captured by our SIMS analyses, which yielded $\delta^{13}C_{org}$ values as low as −42‰. One possible explanation for the inconsistency between $\delta^{13}C_{org}$ values obtained via SIMS measurements, some of which are very low, and the comparatively higher values obtained using bulk techniques, is that only the largest organic domains were measured by SIMS. If sub-micron carbonaceous particles are present, they are too small to be targeted by our SIMS measurement technique, and due to their small size they are also likely to be more susceptible to isotopic re-equilibration with surrounding carbonate mineral phases. Such particles may be present in the D3 dolomite that contributed organic matter to bulk analyses. We intentionally avoided this mineral phase during our SIMS work due both to the absence of large organic domains and to our interpretation of a late diagenetic/metamorphic origin for this phase. Variations in peak characteristics observed in Raman spectra are consistent with structural and chemical variability of OM, but may also relate to alteration of OM due to sample preparation (Beyssac et al., 2003; Lepot et al., 2013) or laser heating (Morishita et al., 2011). Genuine structural and chemical variability could also be induced by variable post-depositional alteration controlled by proximity to hydrothermal veinlets, which are not always obvious in outcrop, hand samples and thin sections (cf. Sforna et al., 2014).

$\delta^{13}C_{carb}$ values for least-altered dolomite phases cluster around a mean of +3.0‰, implying the dissolved inorganic carbon (DIC) that served as a food source for autotrophs was enriched in ^{13}C compared to most carbonate precipitated in open marine conditions. $\delta^{13}C_{org}$ values lower than ∼−37‰ have generally been attributed to the secondary cycling of carbon processed by methane cycling microbes, which impart a strong fractionation (e.g. Hayes, 1994; Eigenbrode and Freeman, 2006). Using the mean $\delta^{13}C_{carb}$ value obtained from microsampled analyses of D1/2 dolomite, 61 of our SIMS data points represent a $\Delta^{13}C_{carb\text{-}org}$ offset of >37‰. Thomazo et al. (2009) reported a bimodal distribution of bulk $\delta^{13}C_{org}$ values from Neoarchean rocks, with the lower peak clustering around a value of −44‰, and Williford et al. (2016) reported a similar distribution of SIMS $\delta^{13}C_{org}$ values correlated to textural variations observed in organic domains in rocks of the same age. Lower values were interpreted in both cases as representing a methanotrophic source or mixing between an autotrophic source and a contribution from methanotrophs.

Alternatively, Slotznick and Fischer (2016) recently suggested that extremely ^{13}C-depleted organic carbon reported from Neoarchean formations worldwide may have been produced by the Wood-Ljungdahl pathway, which could have supported a heterotrophic metabolism capable of significantly further fractionating OM produced by autotrophs utilizing the CBB cycle. Freude and Blaser (2016) observed modern acetogenic bacteria imparting ^{13}C fractionations of up to −69‰ to their product acetate, lending some support to this hypothesis. However, due to the closed nature of the laboratory-based system observed by Freude and Blaser (2016), the CO_2 reservoir became enriched in ^{13}C. Fractionations were measured with respect to this reservoir; smaller fractionations may be expected in natural environments where the isotopic composition of the inorganic carbon reservoir is buffered by atmospheric CO_2. Slotznick and Fischer (2016) argued that carbonates formed in associ-

ation with methane cycling microbial systems are expected to preserve very low $\delta^{13}C_{carb}$ values (which are not typically observed in Archean carbonates preserving highly ^{13}C-depleted organic carbon), but it is unclear whether buffering by a large DIC reservoir may account for the values reported here and from younger units.

Autotrophs utilizing the Wood-Ljungdahl pathway to fix CO_2 directly are known to impart fractionations of 30–40‰ (Preuß et al., 1989; Knoll and Canfield, 1998). This represents a plausible alternative autotrophic source for much of the significantly ^{13}C-depleted organic matter reported from the Strelley Pool Formation. Using the mean $\delta^{13}C_{carb}$ value obtained from microsampled analyses of D1/2 dolomite, 14 of our SIMS data points represent $\Delta^{13}C_{carb\text{-}org}$ offset >40‰, and so exceed the limit thus far observed for organisms utilizing this pathway in conditions representative of natural environments. These values are also beyond the range of fractionation expected for autotrophs utilizing the CBB cycle. They are however well within the range of fractionations observed for methane cycling microbial systems where methanotrophs carry, and sometimes increase, the isotopic fractionation of substrate methane into their biomass (e.g. Orphan et al., 2001). We thus consider the available evidence to be consistent with the operation of at least one autotrophic, or, more likely, heterotrophic metabolism, in addition to the CBB cycle, in the early Archean.

ACKNOWLEDGEMENTS

We thank Kouki Kitajima and John Valley at the University of Wisconsin for their assistance with SIMS analyses and Lora Wingate at the University of Michigan for assistance with carbonate isotope analyses. WiscSIMS is supported by National Science Foundation (EAR-1355590) and the University of Wisconsin, Madison. This material is based upon work supported by the National Aeronautics and Space Administration under Grant NNA13AA94A issued through the Science Mission Directorate. Nicola Ferralis acknowledges support from Shell Oil Company under the MIT Energy Initiative. Roger Summons and Emily Matys were supported by the Simons Foundation via the Simons Collaboration on the Origins of Life. Part of this work was performed at the Jet Propulsion Laboratory, California Institute of Technology, under a grant from the National Aeronautics and Space Administration. We also thank three anonymous reviewers for their improvements to this manuscript.

APPENDIX A. SUPPLEMENTARY MATERIAL

Supplementary data associated with this article can be found, in the online version, at https://doi.org/10.1016/j.gca.2017.11.028.

REFERENCES

Allwood A., Clark B., Flannery D., Hurowitz J., Wade L., Elam T., Foote M. and Knowles E. (2015) Texture-specific elemental analysis of rocks and soils with PIXL: The Planetary Instrument for X-ray Lithochemistry on Mars 2020, Aerospace Conference, 2015 IEEE, pp. 1–13.

Allwood A. C., Grotzinger J. P., Knoll A. H., Burch I. W., Anderson M. S., Coleman M. L. and Kanik I. (2009) Controls on development and diversity of Early Archean stromatolites. *Proc. Natl. Acad. Sci.* **106**, 9548–9555.

Allwood A. C., Kamber B. S., Walter M. R., Burch I. W. and Kanik I. (2010) Trace elements record depositional history of an Early Archean stromatolitic carbonate platform. *Chem. Geol.* **270**, 148–163.

Allwood A. C., Walter M. R., Burch I. W. and Kamber B. S. (2007) 3.43 billion-year-old stromatolite reef from the Pilbara Craton of Western Australia: ecosystem-scale insights to early life on Earth. *Precambr. Res.* **158**, 198–227.

Allwood A. C., Walter M. R., Kamber B. S., Marshall C. P. and Burch I. W. (2006) Stromatolite reef from the Early Archaean era of Australia. *Nature* **441**, 714–718.

Beyssac O., Goffé B., Petitet J. P., Froigneux E., Moreau M. and Rouzaud J. N. (2003) On the characterization of disordered and heterogeneous carbonaceous materials by Raman spectroscopy. *Spectrochim. Acta Part A Mol. Biomol. Spectrosc.* **59**(10), 2267–2276.

Catling D. C., Zahnle K. J. and McKay C. (2001) Biogenic methane, hydrogen escape, and the irreversible oxidation of early Earth. *Science* **293**, 839–843.

Duda J.-P., Van Kranendonk M. J., Thiel V., Ionescu D., Strauss H., Schäfer N. and Reitner J. (2016) A rare glimpse of Paleoarchean Life: geobiology of an exceptionally preserved microbial mat facies from the 3.4 Ga Strelley Pool Formation, Western Australia. *PLoS ONE* **11**, e0147629.

Eigenbrode J. L. and Freeman K. H. (2006) Late Archean rise of aerobic microbial ecosystems. *Proc. Natl. Acad. Sci.* **103**, 15759–15764.

Ferralis N., Matys E. D., Knoll A. H., Hallmann C. and Summons R. E. (2016) Rapid, direct and non-destructive assessment of fossil organic matter via microRaman spectroscopy. *Carbon* **108**, 440–449.

Fischer W. W., Schroeder S., Lacassie J. P., Beukes N. J., Goldberg T., Strauss H., Horstmann U. E., Schrag D. P. and Knoll A. H. (2009) Isotopic constraints on the Late Archean carbon cycle from the Transvaal Supergroup along the western margin of the Kaapvaal Craton, South Africa. *Precambr. Res.* **169**, 15–27.

Freude C. and Blaser M. (2016) Carbon isotope fractionation during catabolism and anabolism in acetogenic bacteria growing on different substrates. *Appl. Environ. Microbiol.* **82**, 2728–2737.

Hallmann C., Kelly A. E., Gupta S.N. and Summons R.E. (2011) Reconstructing deep-time biology with molecular fossils. Quantifying the Evolution of Early Life. Springer, pp. 355–401.

Hayes J. M. (1994) Global methanotrophy at the Archean-Proterozoic transition. In *Early life on Earth: Nobel Symposium 84* (ed. S. Bengston). Columbia University Press, New York, pp. 220–236.

Hickman A. (2008) Regional review of the 3423–3350 Ma Strelley Pool Formation, Pilbara Craton, Western Australia. *West Australia Geolog Surv Rec* **2008**, 15.

Hinrichs K.-U., Hayes J. M., Sylva S. P., Brewer P. G. and DeLong E. F. (1999) Methane-consuming archaebacteria in marine sediments. *Nature* **398**, 802–805.

Hofmann H. J., Grey K., Hickman A. H. and Thorpe R. I. (1999) Origin of 3.45 Ga coniform stromatolites in Warrawoona Group, Western Australia. *Geol. Soc. Am. Bull.* **111**, 1256–1262.

Kita N. T., Ushikubo T., Fu B. and Valley J. W. (2009) High precision SIMS oxygen isotope analysis and the effect of sample topography. *Chem. Geol.* **264**, 43–57.

Kiyokawa S., Ito T., Ikehara M. and Kitajima F. (2006) Middle Archean volcano-hydrothermal sequence: bacterial microfossil-bearing 3.2 Ga Dixon Island Formation, coastal Pilbara terrane, Australia. *Geol. Soc. Am. Bull.* **118**, 3–22.

Knoll A. H. and Canfield D. E. (1998) Isotopic inferences on early ecosystems. *Paleontological Soc. Pap.* **4**, 212–243.

Lepot K., Williford K. H., Ushikubo T., Sugitani K., Mimura K., Spicuzza M. J. and Valley J. W. (2013) Texture-specific isotopic compositions in 3.4 Gyr old organic matter support selective preservation in cell-like structures. *Geochim. Cosmochim. Acta* **112**, 66–86.

Leslie S. A. and Mitchell J. C. (2007) Removing gold coating from SEM samples. *Palaeontology* **50**, 1459–1461.

Lindsay J. F., Brasier M. D., McLoughlin N., Green O. R., Fogel M., Steele A. and Mertzman S. A. (2005) The problem of deep carbon—an Archean paradox. *Precambr. Res.* **143**, 1–22.

Lollar B. S. and McCollom T. M. (2006) Biosignatures and abiotic constraints on early life. *Nature* **444**, E18.

Lowe D. R. (1980) Stromatolites 3400-Myr old from the Archean of Western Australia. *Nature* **284**, 441–443.

Lowe D. R. (1994) Abiological origin of described stromatolites older than 3.2 Ga. *Geology* **22**, 387–390.

Lucchese M. M., Stavale F., Ferreira E. M., Vilani C., Moutinho M., Capaz R. B., Achete C. and Jorio A. (2010) Quantifying ion-induced defects and Raman relaxation length in graphene. *Carbon* **48**, 1592–1597.

Maslova O., Ammar M., Guimbretière G., Rouzaud J.-N. and Simon P. (2012) Determination of crystallite size in polished graphitized carbon by Raman spectroscopy. *Phys. Rev. B* **86**, 134205.

Morishita K., Nara M., Amari S. and Matsuda J. I. (2011) On the effect of laser-induced heating in a raman spectroscopic study of carbonaceous material in meteorite. *Spectrosc. Lett.* **44**(7–8), 459–463.

Melezhik V. A., Fallick A. E., Medvedev P. V. and Makarikhin V. V. (2001) Palaeoproterozoic magnesite: lithological and isotopic evidence for playa/sabkha environments. *Sedimentology* **48**, 379–397.

Oehler D. Z., Robert F., Walter M. R., Sugitani K., Allwood A., Meibom A., Mostefaoui S., Selo M., Thomen A. and Gibson E. K. (2009) NanoSIMS: Insights to biogenicity and syngeneity of Archaean carbonaceous structures. *Precambr. Res.* **173**, 70–78.

Orphan V. J., House C. H., Hinrichs K. U., McKeegan K. D. and DeLong E. F. (2001) Methane-consuming archaea revealed by directly coupled isotopic and phylogenetic analysis. *Science* **293**, 484–487.

Pavlov A. A., Kasting J. F., Eigenbrode J. L. and Freeman K. H. (2001) Organic haze in Earth's early atmosphere: source of low-13C Late Archean kerogens? *Geology* **29**, 1003–1006.

Preuß A., Schauder R., Fuchs G. and Stichler W. (1989) Carbon isotope fractionation by autotrophic bacteria with three different C02 fixation pathways. *Zeitschrift für Naturforschung C* **44**, 397–402.

Rantitsch G., Lämmerer W., Fisslthaler E., Mitsche S. and Kaltenböck H. (2016) On the discrimination of semi-graphite and graphite by Raman spectroscopy. *Int. J. Coal Geol.* **159**, 48–56.

Schidlowski M. (1987) Application of stable carbon isotopes to early biochemical evolution on Earth. *Annu. Rev. Earth Planet. Sci.* **15**, 47.

Schidlowski M. (1988) A 3800-million-year isotopic record of life from carbon in sedimentary rocks. *Nature* **333**, 313–318.

Sforna M. C., Van Zuilen M. A. and Philippot P. (2014) Structural characterization by Raman hyperspectral mapping of organic carbon in the 3.46 billion-year-old Apex chert, Western Australia. *Geochimica et Cosmochimica Acta* **124**, 18–33.

Shields G. and Veizer J. (2002) Precambrian marine carbonate isotope database: Version 1.1. Geochemistry, Geophysics, Geosystems 3.

Slotznick S. P. and Fischer W. W. (2016) Examining Archean methanotrophy. *Earth Planet. Sci. Lett.* **441**, 52–59.

Sugitani K., Lepot K., Nagaoka T., Mimura K., Van Kranendonk M., Oehler D. Z. and Walter M. R. (2010) Biogenicity of morphologically diverse carbonaceous microstructures from the ca. 3400 Ma Strelley Pool Formation, in the Pilbara Craton, Western Australia. *Astrobiology* **10**, 899–920.

Sugitani K., Mimura K., Nagaoka T., Lepot K. and Takeuchi M. (2013) Microfossil assemblage from the 3400Ma Strelley Pool Formation in the Pilbara Craton, Western Australia: Results form a new locality. *Precambr. Res.* **226**, 59–74.

Sugitani K., Mimura K., Takeuchi M., Yamaguchi T., Suzuki K., Senda R., Asahara Y., Wallis S. and Van Kranendonk M. J. (2015) A Paleoarchean coastal hydrothermal field inhabited by diverse microbial communities: the Strelley Pool Formation, Pilbara Craton, Western Australia. *Geobiology* **13**, 522–545.

Thomazo C., Ader M., Farquhar J. and Philippot P. (2009) Methanotrophs regulated atmospheric sulfur isotope anomalies during the Mesoarchean (Tumbiana Formation, Western Australia). *Earth Planet. Sci. Lett.* **279**, 65–75.

Tucker M. E. (1982) Precambrian dolomites: petrographic and isotopic evidence that they differ from Phanerozoic dolomites. *Geology* **10**, 7–12.

Ueno Y., Yamada K., Yoshida N., Maruyama S. and Isozaki Y. (2006) Evidence from fluid inclusions for microbial methanogenesis in the early Archaean era. *Nature* **440**, 516–519.

Ushikubo T., Williford K. H., Farquhar J., Johnston D. T., Van Kranendonk M. J. and Valley J. W. (2014) Development of in situ sulfur four-isotope analysis with multiple Faraday cup detectors by SIMS and application to pyrite grains in a Paleoproterozoic glaciogenic sandstone. *Chem. Geol.* **383**, 86–99.

Valley J. W. and Kita N. T. (2009) In situ oxygen isotope geochemistry by ion microprobe. *MAC short course: secondary ion mass spectrometry in the earth sciences* **41**, 19–63.

Van Kranendonk M. J. (2006) Volcanic degassing, hydrothermal circulation and the flourishing of early life on Earth: a review of the evidence from c. 3490–3240 Ma rocks of the Pilbara Supergroup, Pilbara Craton, Western Australia. *Earth-Sci. Rev.* **74**, 197–240.

Van Kranendonk M. J., Webb G. E. and Kamber B. S. (2003) Geological and trace element evidence for a marine sedimentary environment of deposition and biogenicity of 3.45 Ga stromatolitic carbonates in the Pilbara Craton, and support for a reducing Archaean ocean. *Geobiology* **1**, 91–108.

Veizer J. and Hoefs J. (1976) The nature of O18/O16 and C13/C12 secular trends in sedimentary carbonate rocks. *Geochim. Cosmochim. Acta* **40**, 1387–1395.

Wacey D. (2010) Stromatolites in the ~3400 Ma strelley pool formation, Western Australia: examining biogenicity from the macro- to the nano-scale. *Astrobiology* **10**, 381–395.

Wacey D., Kilburn M. R., Saunders M., Cliff J. and Brasier M. D. (2011) Microfossils of sulphur-metabolizing cells in 3.4-billion-year-old rocks of Western Australia. *Nat. Geosci.* **4**, 698–702.

Wacey D., McLoughlin N., Whitehouse M. J. and Kilburn M. R. (2010) Two coexisting sulfur metabolisms in a ca. 3400 Ma sandstone. *Geology* **38**, 1115–1118.

Williford K., Ushikubo T., Lepot K., Kitajima K., Hallmann C., Spicuzza M., Kozdon R., Eigenbrode J., Summons R. and Valley J. (2016) Carbon and sulfur isotopic signatures of ancient life and environment at the microbial scale: Neoarchean shales and carbonates. *Geobiology* **14**, 105–128.

Yoshida A., Kaburagi Y. and Hishiyama Y. (2006) Full width at half maximum intensity of the G band in the first order Raman spectrum of carbon material as a parameter for graphitization. *Carbon* **44**, 2333–2335.

Associate editor: Jochen J. Brocks